Highlights

CIEL*Ch color map for visualization and analysis of sea ice motion

J. Upston, D. Sulsky, J.D. Tucker, Y. Guan

- A novel use of color is presented for scientific analysis and visualization.
- Applications to color encoding of vector fields show utility of the color map.
- Image registration is used to analyze localized sea ice fractures (leads).
- An image registration technique using space filling curves reliably aligns images.
- A new image amplitude metric and image phase measure can be used in parameter calibration.

CIEL*Ch color map for visualization and analysis of sea ice motion

J. Upston[a,*], D. Sulsky[a,b], J.D. Tucker[c], Y. Guan[d]

[a]*Department of Mathematics and Statistics, University of New Mexico, Albuquerque, 87131, NM, USA*
[b]*Department of Mechanical Engineering, University of New Mexico, Albuquerque, 87131, NM, USA*
[c]*Statistical Sciences, Sandia National Laboratories, Albuquerque, 87185, NM, USA*
[d]*Department of Statistics, University of Nebraska, Lincoln, 68583, NE, USA*

Abstract

The International Commission on Illumination (CIE) designed its color space to be perceptually uniform so that a given numerical change in the color code corresponds to perceived change in color. This color encoding is demonstrated to be advantageous in scientific visualization and analysis of vector fields. The specific application is analysis of ice motion in the Arctic where patterns in smooth monthly-averaged ice motion are seen. Furthermore, fractures occurring in the ice cover result in discontinuities in the ice motion. This vector jump in displacement can also be visualized. We then analyze modeled and observed fractures through the use of a metric on the color space, and image amplitude and phase metrics. Amplitude and phase metrics arise from image registration that is accomplished by sampling images using space filling curves, thus reducing the image registration problem to the more reliable functional alignment problem. We demonstrate this through an exploration of the metrics to compare model runs to an observed ice crack.

Keywords: CIELab color space, image registration, space filling curves, visualization

*Corresponding author
Email address: jupston@unm.edu (J. Upston)

1. Introduction

This paper presents tools for analyzing two-dimensional vector fields. These fields arise in meteorology and oceanography, for example. Our particular interest is analyzing sea ice motion in the Arctic, either observed through remote sensing or simulated using computer models. The statistics of scalar quantities are well studied (e.g., [1]), statistical measures applied to vector quantities remains an area of research. Vectors have magnitude and direction, and analysis is further complicated because the direction is a circular quantity [2]. In analyzing sea ice forecasts, Grumbine [3] recommends five skill measures. A combination of skill measures is necessary since each individually gives an incomplete picture for determining how sets of vectors are related. In this paper, we combine three skill measures to form a metric for comparing vector fields. The metric is constructed from properties of a color map. A benefit of this construction is a natural way to visualize the metric.

The International Commission on Illumination (CIE) designed a color space to be perceptually uniform so that a given numerical change in the color code corresponds to a given perceived change in color. We exploit this property of the color space to propose a color map for vectors based on use of the CIE Lightness-Chroma-hue (CIEL*Ch) color space [4]. Within this space, vector magnitude is mapped to the intensity of the color while hue, or the color itself, indicates the direction or vector orientation. Additional information about the vector field can be encoded in the color map by varying the chroma. Due to the design of the CIEL*Ch color space, the L_2 norm on the color encoding induces a metric on vectors. Thus, we have designed a tool where differences in vector fields can be analyzed through differences in color.

A predominant feature of Arctic sea ice, especially in the winter, is the formation of fractures. Fractures can be described by a vector giving the amount of opening and its direction at a given point. However, these fractures exist on curves within a two-dimensional domain and do not fill the entire area. Common point-wise differences and root mean squared (RMS) metrics are flawed when comparing these lower dimensional features within the two-dimensional space. Models that fail to predict these features can have a smaller RMS error than models that predict these features but at a somewhat displaced position or altered orientation than observations indicate. For this reason, Guan et al. [5] introduced the idea of optimally aligning

model output with observed features using image warping techniques. A central contribution of the current paper is to demonstrate that two-dimensional image warping can be reduced to a simpler-to-solve, one-dimensional problem using space filling curves. We further build on our vector color map and distance metric to provide distance measures between images of fractures. The measures are the amount of warping needed to align the images (phase error) and an L_2 distance after alignment (amplitude error). With these measures additional analysis, such as parameter calibration, is possible for fracture models.

In Section 2, we describe the CIEL*Ch color space and the distance metric on that space. The color map induces a corresponding metric on vectors which can be visualized naturally through the color map. Examples of the color map and vector visualization are provided in Sec. 2.1. In particular, Sec. 2.1 uses observations of monthly-averaged, daily ice motion to demonstrate the utility of the metric and its inherent color visualization.

Fracture modeling and visualization is described in Sec. 3. Image warping is introduced in Sec. 3.1 and space filling curves in Sec. 3.2. Space filling curves reduce the image warping problem to one of functional data alignment, which is presented in Sec. 3.3. An example of aligning images containing single cracks is given in Sec. 3.4. Motivated by this example, the definition of an image amplitude metric and phase distance measure are given in Sec. 3.5. The use of space filling curves to reduce image alignment to functional data alignment, the metrics for comparing image features based on image warping, and the color map to visualize metrics are new to this work. Sec. 3.6 demonstrates use of these measures in parameter calibration by parameterizing positions and orientations of cracks in an image. The procedure of registering images using space filling curves is shown to work across the parameter space and the measures are minimized around the correct parameter setting. Section 4 provides concluding comments.

2. Vector Visualization

Vectors are typically visualized using arrows. It can be difficult to visually decipher the contributions of magnitude and direction when comparing two vector fields using arrows [6, 7, 8]. Color is a useful device to aid visual perception. However, the color space could be misleading if not chosen appropriately [7]. We consider the CIE-L*a*b* 1976 color space [4, 7] which is split into three color channels lightness, L^*, the red-green component, a^*,

and the yellow-blue component, b^*. The components a^* and b^* comprise Cartesian coordinates of the chroma and hue. The lightness ranges from 0 to 100, and the a^* and b^* channels range from -100 to 100. This color model is derived specifically so that the L_2 metric on the color components measures closeness in perceived color, a feature not present in more familiar RGB, HSV, or CMYK color models [7]. The L_2 distance metric between two colors encoded by the triples (L_1^*, a_1^*, b_1^*) and (L_2^*, a_2^*, b_2^*) is denoted by ΔE and given by

$$\Delta E = \sqrt{(L_1^* - L_2^*)^2 + (a_1^* - a_2^*)^2 + (b_1^* - b_2^*)^2}. \tag{1}$$

The metric ΔE can also be written in the cylindrical CIEL*Ch formulation,

$$\Delta E = \sqrt{(L_1^* - L_2^*)^2 + (C_1 \cos h_1 - C_2 \cos h_2)^2 + (C_1 \sin h_1 - C_2 \sin h_2)^2}. \tag{2}$$

The lightness L^* remains unchanged, but the polar coordinates of chroma, C, and hue, h, are used instead of the Cartesian coordinates a^* and b^*. The usual transformation holds

$$C = \sqrt{a^{*2} + b^{*2}}, \qquad h = \arctan(b^*/a^*). \tag{3}$$

Lightness determines how dark or light the color is and chroma represents how vivid or dull the color is, while hue is the change in color. Lightness and chroma have a value from 0 to 100, and hue varies from $-\pi$ to π.

The orientation of a vector is given by the angle it makes to the x-axis, a periodic quantity for two-dimensional vector fields. The periodic structure has no beginning or end. In a standard color map, the arbitrary end points of a color map must be the same color to avoid the appearance of a discontinuity [9]. In constructing a color map for vectors, the natural channel to deal with the periodicity of the orientation is the hue, which is also periodic. Therefore one option is to think of the lightness as the magnitude of the vector and the hue as the orientation of the vector, with a constant chroma. In order to assign a color to a vector in a vector field, the set of vectors should be scaled so that magnitudes have valid lightness values in the range $[0, 100]$. Thus, two-dimensional vectors with polar coordinates (r, θ) map to colors with $L^*(r, \theta) = r$, $h(r, \theta) = \theta$, with constant chroma C. The color metric on two vectors, (r_1, θ_1) and (r_2, θ_2), reduces to

$$\Delta E = \sqrt{(r_1 - r_2)^2 + 4C^2 \sin^2((\theta_1 - \theta_2)/2)}. \tag{4}$$

It is straightforward to show that ΔE defined in Equation [4] is a metric on the space of two-dimensional vectors. For vectors, ΔE measures differences in vector magnitude and vector orientation. Notice that the value of constant chroma can be chosen to weight each of the these components stored in L^* and h, providing a family of metrics on the color space. For example if the chroma is zero then no information about the orientation is used and only magnitude of the vector is displayed in a gray scale image. Whereas if chroma is 100, the orientation is heavily weighted, about twice the value of the magnitude in the lightness channel. A chroma of 50 roughly weights the magnitude and orientation equally.

In our applications, we have encountered situations where it is convenient and informative to employ the flexibility in the CIEL*Ch color model provided by utilizing non-constant chroma. Non-constant chroma in the color space creates color mappings that enhance or understate aspects of a vector or a group of vectors. One such mapping of two-dimensional vectors with polar components (r, θ) scaled so that $r \in [0, 1]$, is

$$\begin{aligned} L^*(r, \theta) &= 50\sqrt{3}r \\ C(r, \theta) &= 50r \\ h(r, \theta) &= \theta. \end{aligned} \tag{5}$$

Scaling of vectors is accomplished using the maximum magnitude of the data or a threshold to compare multiple data sets consistently. The color map, Equation [5], maps two-dimensional vectors to a cone-shaped subspace of the CIEL*Ch color space. The constants are chosen so that the color difference metric, ΔE, has the same value for two vectors of equal magnitude but opposite orientation and two vectors of the equal orientation and opposite magnitude.

The color map, Equation [5], can be illustrated without loss of generality by examining vectors in the unit disk. Figure 1 shows the color representation for vectors in this disk, with color assigned to the polar representation of the two-dimensional vector. The scaling of L^* and C with r results in darker, less vivid colors for smaller vectors. With the chroma linearly dependent on the vector magnitude, colors are centered around black, representing the absence of color. There is no natural ordering of hue [7]. Hue can be shifted in equation [5] so that a specific color represents a particular angle, e.g. green for 0°, by defining a new hue, $H(r, \theta) = \theta + \pi$. An appropriate shift would be application dependent. We use the color wheel in Figure 1(a) as a legend

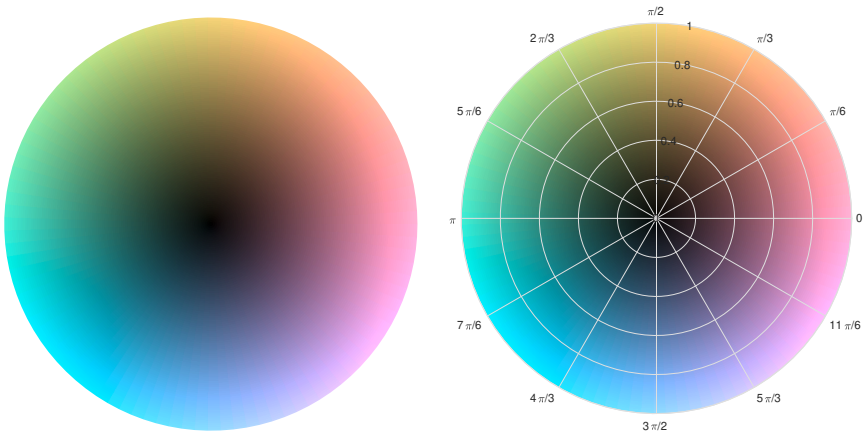

(a) (b)

Figure 1: Polar representation of vector color map

in other figures instead of the usual color bar.

The color metric corresponding to the map Equation [5] can be written in the form

$$\begin{aligned} \Delta L^* &= 50\sqrt{3}|r_1 - r_2| \\ \Delta C &= 50\sqrt{(r_1 - r_2)^2 + 4r_1 r_2 \sin^2((\theta_1 - \theta_2)/2)} \\ \Delta h &= \theta_1 - \theta_2 \\ \Delta E &= \sqrt{\Delta L^{*2} + \Delta C^2 \cos^2(\Delta h) + \Delta C^2 \sin^2(\Delta h)}. \end{aligned} \tag{6}$$

It is again straightforward to verify that Equation [6] is a metric on the space two-dimensional vectors. For colors, ΔE is still the L_2 metric, Equation [1] or Equation [2], but interpreted as a metric on vectors, ΔE is non-Euclidean. However, vectors close in this metric are mapped to colors that are perceptually close in the color space. An interpretation of this metric in terms of skill measures is described next.

Equation [6] is written in a form to suggest a visualization method for vector differences, where the L*Ch color code is taken to be $(\Delta L^*, \Delta C, \Delta h)$. If the vector difference represents a measurement error, this novel color coding for vector differences combines information from three skill measures, the magnitude difference (ΔL^*), direction error (Δh), and (ΔC). The last of these contributions is not as straightforward as the other two. It contains

information about the magnitude of the vectors themselves, in addition to the differences in magnitude and direction. If, for example, r_1 is much larger than r_2 then $\Delta C \approx 50 r_1$ reflects the larger vector size. A vector difference that has similarly large magnitude vectors with differing orientation would appear dark, due to minimal magnitude difference, but have a vivid color due to the differing orientation. However, for the case with similarly small magnitude vectors and differing orientation, the result would be a dark and dull color, near black.

The mapping, Equation [5], enables both a vector field and the difference between vector fields to be shown as a unique and meaningful L*Ch color code. In subsequent sections, we rely on the norm ΔE to quantify differences in vectors and differences in images.

2.1. Arctic Motion Data Visualization and Analysis

An illustration of the color map, Equation [5], is obtained by visualizing monthly-averaged daily Arctic ice motion vectors on a 100 km SSM/I grid. The data are available from NSIDC [10]. Zhao and Liu [11] study the circulation regimes and winter-to-winter variability of Arctic sea-ice motion. They find that the mean Arctic sea-ice motion during the winter seasons from 1988 to 2003 has two distinct features: the Beaufort Gyre and a cyclonic circulation system in the Eurasian Basin moving ice from the Laptev Sea to Fram Strait.

There are several methods available for analyzing and visualizing vector fields, e.g. [6]. Each method has its own advantages and disadvantages. Four methods are applied to the Arctic sea-ice motion field in January of 2004 and shown in Figure 2. Figure 2(a) uses quiver arrows to show the displacement field. This is a discrete representation of the vector field. The direction of a vector is given by the arrow orientation and the magnitude is given by the size of the arrow. When there is a large range of magnitudes, small magnitude arrows can be difficult to discern. The vector field often has to be subsampled in order to effectively see the arrows. Munzner [7] also notes that the accuracy of our perception of angle is not uniform. 'We have very accurate perceptions of angles near the exact horizontal, vertical, or diagonal positions, but accuracy drops off in between them. We can tell 89° from 90°, 44° from 45°, and 1° from 0°; however, we cannot tell 37° from 38°'.

The remaining three methods provide a continuous representation of the flow. The Line Integral Convolution (LIC) in Figure 2(b) shows the flow but not its direction. However, the LIC is particularly useful in identifying

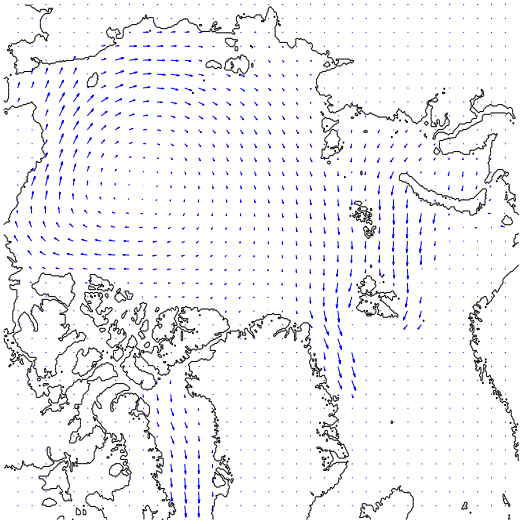

(a) Quiver

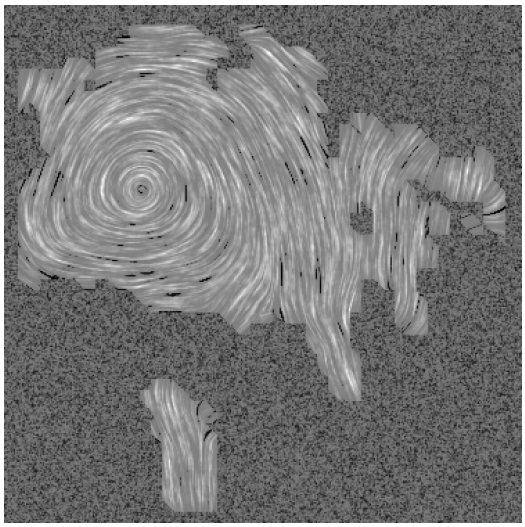

(b) LIC

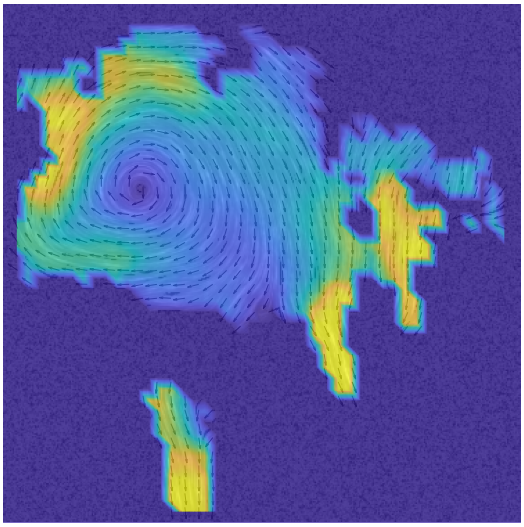

(c) LIC with Magnitude Underlay

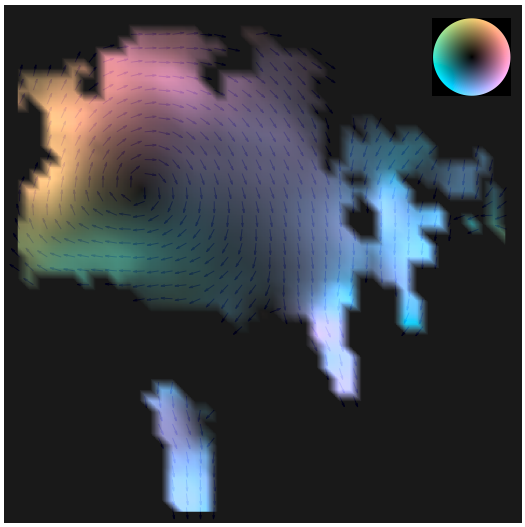

(d) Vector Color Map

Figure 2: Vector visualization comparison

critical points in otherwise smooth flow fields [6] – the gyre center in this view is readily apparent. The color scale in Figure 2(b) represents different flows and does not represent the magnitude of the flow. The LIC can be enhanced using the overlay and underlay techniques from [12]. Figure 2(c), uses the standard parula[1] color map to represent the flow magnitude and the flowlines in the underlay LIC, and an overlay of the orientation arrows to show the direction of the flow. The combination captures information about the field within one image through these independent layers. Lastly we show the vector color map given by Equation [5] to display the Arctic vector field in Figure 2(d). The brighter areas of this plot indicate large vector magnitude and the hues represent the orientation. To help guide the reader in interpreting the hue, we overlay quiver arrows. The chroma, being also a function of vector magnitude, de-emphasizes the color when the vector magnitude is small. Figure 2(d) captures the gyre, has brighter areas to highlight larger magnitude vectors as in Figure 2(c), and shows flow direction through the hue or overlaid arrows.

2.2. Arctic Motion Comparison

Returning to the analysis of Zhao and Liu [11], we can look at the strengths and sizes of the Beaufort Gyre and cyclonic flow, and how they change from season to season. We take as an example, January 1994 ice motion, depicted in Figure 3(a), which shows a Beaufort Gyre, while Figure 3(b) shows January 1995 ice motion which has a weak Beaufort Gyre and a strong cyclonic motion.

Figures 3(a,b) show the CIEL*Ch rendering of ice motion vectors, using the color map Equation [5]. The cone structure of the color map dulls small vector magnitudes. The gyre in Figure 3(a) has a dark center since vector magnitude is relatively smaller. Around the dark center is a variation in hue indicating the varying vector orientation of flow around the gyre. The brighter patches of color are regions where vector magnitude is largest. The predominantly pink color in the central Arctic shown in Figure 3(b) indicates vectors oriented near zero degrees, a mainly horizontal flow. Both Figures 3(a,b) have bright blue areas around Greenland indicating large southward flow of ice being exported from the Arctic.

The color rendering of Figures 3(a,b) reveals the distinct features of ice

[1]The parula map is the current default map in Matlab. It is not perceptually uniform.

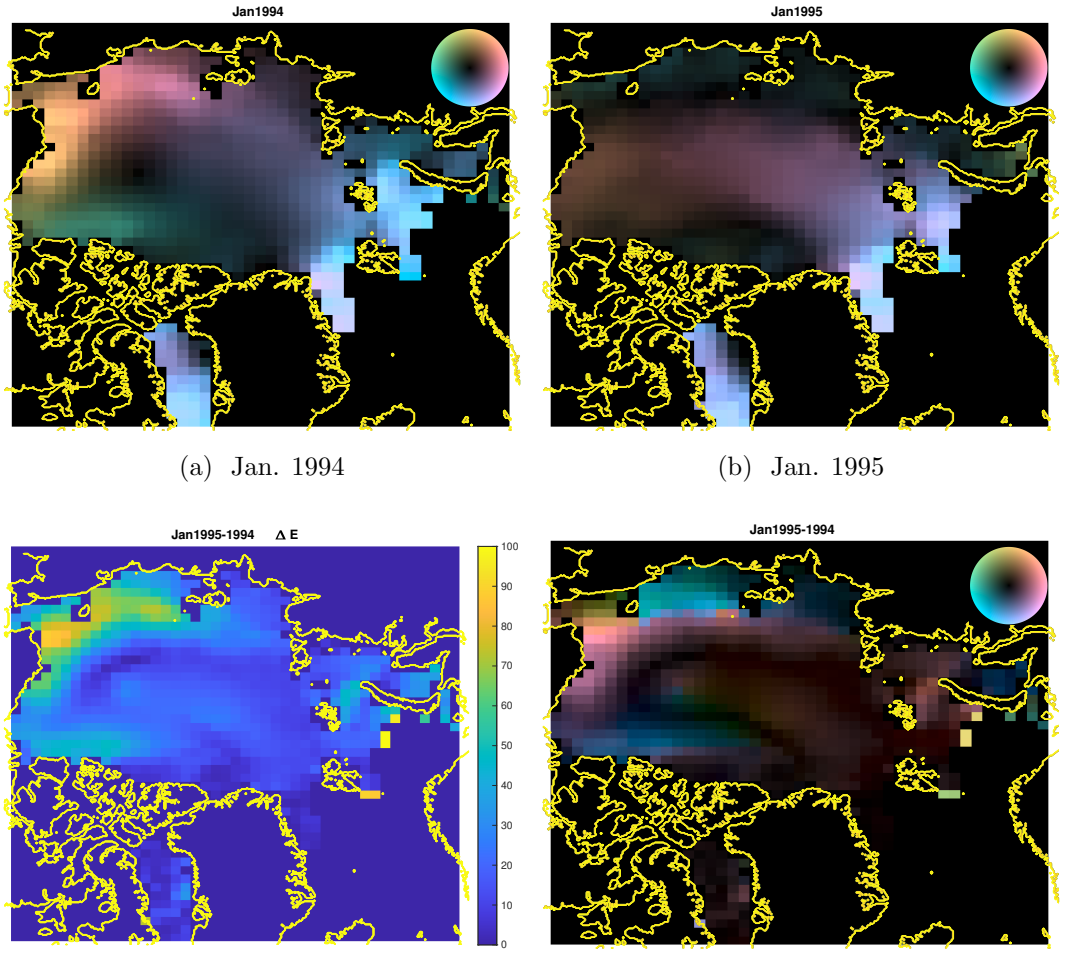

(a) Jan. 1994

(b) Jan. 1995

(c) ΔE for Jan. 1995-1994

(d) Color Difference Map for Jan. 1995-1994

Figure 3: Visualization of Arctic ice motion in L*Ch color space.

motion described in [11]. The difference between these two patterns of ice motion is quantified by the color metric. A contour plot, using the parula color map, of ΔE for the difference of vectors in Figures 3(a,b) is shown in Figure 3(c). Large values of ΔE, for example off the coast of Alaska and Eastern Siberia, indicate either large magnitude and/or large orientation differences. To discern which attribute is contributing most to the metric, the difference color map, Equation [6], can be used. The rendering is displayed in Figure 3(d). Near the coast of Alaska, the bright pink areas indicate near zero orientation difference, but large magnitude difference contributing to ΔE. Near the Eastern Siberian coast, the large difference has a blue hue, indicating both an orientation difference of about $-3\pi/4$ and a magnitude difference in the vectors. Duller colors correspond to smaller magnitude differences and orientation differences whose size is indicated by the hue. Vectors of similar size around Greenland have a small difference and are rendered as dark, dull areas in Figure 3(d). Parts of the Beaufort Gyre that align with the cyclonic motion are also dark, dull regions in the figure. The region in the center of the gyre in Figure 3(a) has an orientation difference when compared to the cyclonic motion in Figure 3(b), since the cyclonic motion is primarily unidirectional. Figure 3(d) shows differences in hue where the center of the gyre would be, with the darker colors representing small magnitude differences.

3. Fracture Modeling Verification

The monthly-averaged Arctic motion of the last section results in smooth vector fields where it makes sense to compare fields by simple differences. Visualization techniques that rely on smooth flow fields, like LIC are also appropriate. However, stresses on the ice, particularly in the winter, cause the ice cover to fracture and open up into leads. Shifting stresses can later cause convergent flow with refrozen leads being crushed into pressure ridges. Thus, ice motion influences ice mass balance in the Arctic, with leads playing an important role. Lead formation, or fracture, implies that the displacement field has a jump singularity.

Modeling fracture formation in sea ice is a nascent area of research with no established methods for visualization and analysis. The jump in displacement is a vector quantity. The magnitude of the vector is the size of the jump, and the direction is the direction of crack opening. The direction of the jump is measured by the angle that the normal to the crack makes to

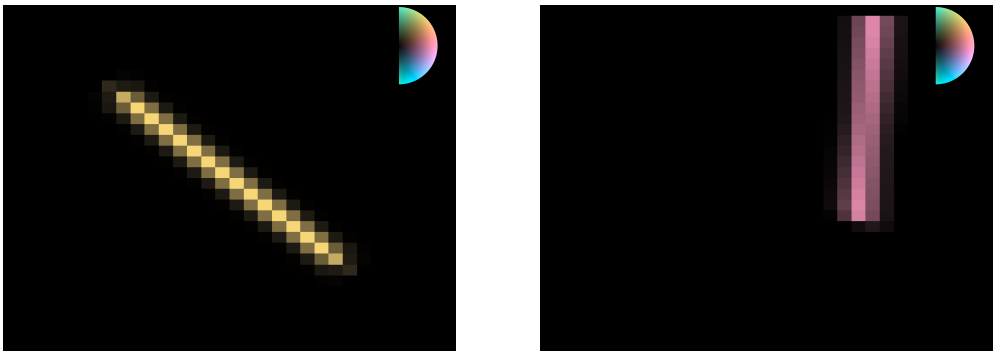

(a) Observation (b) Simulation

Figure 4: Visualization of cracks.

the x-axis. The distribution of these fractures in space, the distribution of sizes, and the distribution of orientations are quantities of interest. It is also of interest to have a metric to compare two fractures, say one predicted from a simulation and the other observed. A simple difference between two images that contain fractures will be meaningless since the fractures will not generally be coincident, aligned, or the same size and shape.

Since the displacement jump associated with a fracture is a vector quantity, it can be visualized using the CIEL*Ch color map. The orientation angles fall uniquely in the range $(-\pi/2, \pi/2]$ and are mapped to a hue in the color map by doubling their value. Figure 4(a) shows a sketch of a straight crack with constant jump magnitude. The orientation is indicated by the yellow coloring associated with the normal to the crack being at an angle of $\pi/4$ to the horizontal. Similarly, Figure 4(b) depicts a straight crack with a pink color denoting an orientation at zero. For the purposes of this illustration, Figure 4(a) will be thought of as an observed crack and Figure 4(b) as the result of a simulation.

Since the displacement jump due to a crack is localized along a curve, fractures cannot be compared using simple differences between the two localized displacement fields since the fractures do not align. Guan et al. [5] introduced the idea of image warping as a way to compare localized fractures in two-dimensional images. This section uses the idealized problem sketched in Figure 4 to illustrate use of (i) image warping to align localized features for comparison, (ii) space-filling curves to reduce image warping to the easier

problem of functional alignment, (iii) metrics for comparison of image features based on image warping, and (iv) the CIEL*Ch color map to visualize the metrics.

3.1. Image Warping

An image is a rectangular array of pixels, each pixel having a color. Image registration, finding a correspondence between pixels across images, is a standard problem in image processing (see [13] for a review). Recently, the concept of warping images for registration using metrics has become increasingly popular given the properties it provides (Beg et al. [14], Tagare et al. [15], Vercauteren et al. [16], Xie and Srivastava [17]). In [5] we propose using amplitude and phase metrics, introduced by Xie and Srivastava [17], which are proper distances in the space of images. The phase metric gives a measure of how much warping is required to register geometric features. The other, amplitude metric, gives a measure of the pixel intensity differences, if any, after an optimal warping has been applied. The combination of the measures allows one to determine how well a model is reproducing geometric features or coherent structures. A low amplitude metric, for instance, implies there is a smooth deformation from one image to the other, meaning a geometric feature is likely captured but perhaps misaligned. The magnitude of the phase metric gives a measure of how misaligned the feature is. In contrast, a high amplitude metric implies the geometric features of the two images are inconsistent and are not captured by the model.

Mathematically, the image warping process requires determining an optimal, boundary preserving diffeomorphism, γ^*, that maps one image to another under the so-called q-map of the image. The reader is referred to [17] and [5] for details. However, difficulties arise with this construct. The gradient descent used to determine the optimal warping function is difficult to control. It is sensitive to step size and the number of basis functions used to represent γ^* in its orthonormal expansion. The extrinsic metric using the q-map gives a nice metric for computing the distance between images, but further statistical analysis, such as principal component analysis, becomes hard due to the fact that the inverse mapping is not available in closed form. The restriction to boundary-preserving diffeomorphisms also constrains the amount of motion available for two-dimensional image alignment.

3.2. Space Filling Curves

The same difficulties that arise in warping two-dimensional images do not arise in the amplitude and phase separation of functional data [18]. In order to transform the image registration problem to one of function registration, we introduce the idea of sampling the image using space filling curves (SFC).

A naive way to covert a two dimensional image to a one dimensional image is by sweeping through the rows, one row at a time, or through the columns, one column at a time, and concatenating them into a single row or column. However pixels that are in the same column but in different rows are far apart within this one dimensional construction. It is useful to try and preserve locality when we transform the images to one dimension, *i.e.,* points that are close in the two dimensional image are also close in the one dimensional space. Space filling curves provide a mechanism to map multidimensional space into one dimensional space [19] which approximately preserves locality.

There are many ways to construct a space filling curve, but the most widely used in two dimensions is the Hilbert curve. Compared to other space filling curves, it has higher autocorrelation [20] and its shape is not biased toward one dimension over another [21]. Space filling curves are built by a recursive algorithm that gets to finer resolution and fills out the domain with increasing order, n, with the entire two-dimensional region traversed as $n \to \infty$. Applied to dimension reduction for images, the order of the space filling curve is finite since only the finite number of pixels in the image need to be traversed. We will use the notation SFC(n) for a space filling curve of finite order, n. We often only need order $n = 5 - 7$ to sample the image adequately. Figures 5(a,b) show a Hilbert curve of order 5 superimposed on the cracks from Figure 4. The endpoints of the Hilbert curve in this example are in the upper and lower left-hand corners. The space filling curve provides a parameterization $\mathbf{x}(s) = (x(s), y(s))$, $s \in [0, 1]$ for the points $\mathbf{x} = (x, y)$ in the image. A variant of the Hilbert curve algorithm creates a looped (periodic) Hilbert curve, also known as the Moore curve with $x(0) = x(1)$ and $y(0) = y(1)$. We employ looped variations and rotations of the curve depicted in the figure to sample images. The rotations place the starting and ending points in different corners of the image.

3.3. Functional Data Alignment

Once the two dimensional image is mapped to one dimension via the SFC(n), we can use functional alignment to compare images. Let $\mathcal{F}$ be

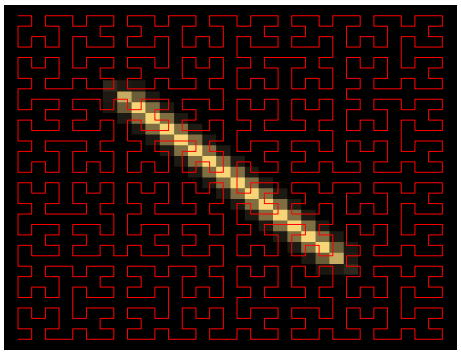

(a) Observation

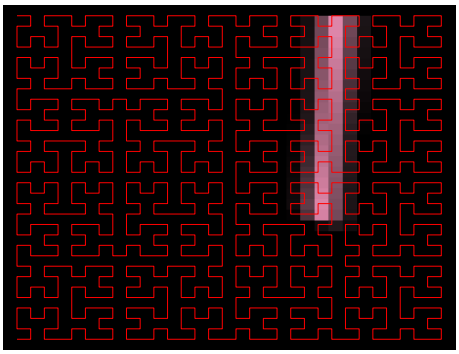

(b) Simulation

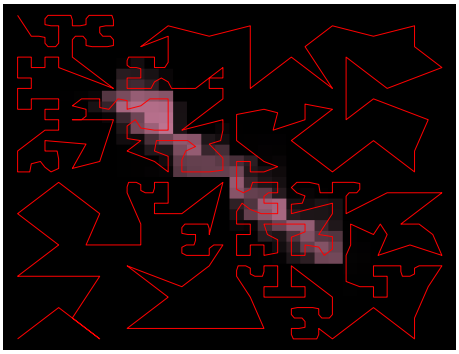

(c) Warped Simulation

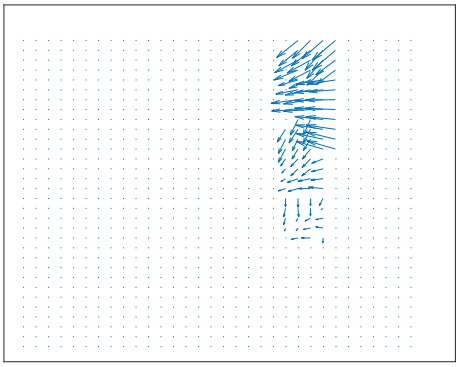

(d) Simulation to Observation Displacement

Figure 5: Visualization of the cracks with Hilbert SFC(5) and warping application.

the set of absolutely continuous functions with domain $[0,1]$. In functional alignment, given functions, f_1, f_2, in $\mathcal{F}$, the goal is to optimally align f_2 to f_1. Alignment or warping functions, γ, are boundary preserving diffeomorphisms, $\gamma \in \Gamma = \{\gamma : [0,1] \to [0,1], \gamma(0) = 0, \gamma(1) = 1, \gamma \text{ a diffeomorphism}\}$. For any $f \in \mathcal{F}$ and $\gamma \in \Gamma$, the composition, $f \circ \gamma$ denotes the warping of f, by γ.

Srivastava and Klassen [22] introduce use of the square root slope function (SRSF) of f in the cost function defining the optimal warp γ^*. The SRSF of f is $q : [0,1] \to \mathbb{R}$ with $q(f) = \text{sign}(\dot{f})\sqrt{\dot{f}}$. Note that if $f \in \mathcal{F}$ then $q \in L_2$. Moreover, for any $q \in L_2$ and $t \in [0,1]$, $f(t)$ can be obtained from q through the relation $f(t) = f(0) + \int_0^t q(s)|q(s)|ds$ since the integrand is $\dot{f}(s)$. If we warp f by γ, the SRSF of $f \circ \gamma$ is $(q, \gamma) = q(\gamma)\sqrt{\dot{\gamma}}$, and it can be shown [23, 24, 22] that $\|q_1 - q_2\| = \|(q_1, \gamma) - (q_2, \gamma)\|$ where q_1, q_2 are SRSFs of f_1, f_2. This isometry property suggests a cost function defining the optimal warping function given by $\gamma^* = \text{arginf}_{\gamma \in \Gamma} ||q_1 - (q_2, \gamma)||$. That is, we align the SRSFs of any two functions first and then map back to $\mathcal{F}$ to obtain the registered functions. The optimization problem is solved using standard dynamic programming.

The isometry property leads to a distance metric between functions f_1, f_2 that is invariant to their warpings [24]. The amplitude distance, d_a, is the difference between the functions once they are aligned and the phase distance, d_p, measures how much warping is needed to align the functions. These distances are defined as

$$\begin{aligned} d_a(f_1, f_2) &= \inf_{\gamma \in \Gamma} ||q_1 - (q_2, \gamma)|| \\ d_p(\gamma) &= \arccos\left(\int_0^1 \sqrt{\dot{\gamma}}\, dt\right). \end{aligned} \tag{7}$$

3.4. Image Warping Example

Returning to the example shown in Figure 5, points along the SFC(n), $\mathbf{x}(s) = (x(s), y(s))$, are given a color encoded by the lightness-chroma-hue triplet, $(l(s), c(s), h(s))$. The color is assigned based on the vector jump in displacement field at that point. The lightness channel in the color map corresponds to the magnitude of the vector. Thus, we can view the lightness as also parameterized by s and obtain a function $l(s)$, $s \in [0,1]$, giving the image lightness. If we align the lightness functions of the two images we are aligning the vector magnitude of the jump in displacement through its

color space representation. More precisely, the space filling curve of finite order n is defined by $N = 2^{2n}$ nodes. The lightness $l(s)$ is the piecewise linear function that continuously joins the nodal values $l(s_i)$, as such $l(s) \in \mathcal{F}$. Once the optimal warping based on the lightness channel is found we can apply that warping to the other color channels. Figure 5(c) shows the warped space filling curve that results from aligning the simulation to the observation, along with the aligned crack. In mapping simulation lightness, $l_2(s)$, to the observation lightness, $l_1(s)$, Figure 5(c) shows the color $(l_2 \circ \gamma^*(s), c_2 \circ \gamma^*(s), h_2 \circ \gamma^*(s))$ plotted at $\mathbf{x}(s)$. Figure 5(c) shows the pink, vertical, simulation crack shown in Figure 5(b) aligned with the observation crack from Figure 5(a) through this process.

Even though the space filling curves try to preserve locality it can still be the case that points close in 2D are not necessarily close in 1D. In order to mitigate biases that might be introduced by choosing one space filling curve overlaid on a specific image, we sample the image with a few different variations of space filling curves and use the best sampling for that image. Specifically, we take $\frac{k\pi}{2}$, where $k = 1, 2, 3, 4$, rotations of the Hilbert curve and it's looped variant the Moore curve, for a total of 8 different 1D representations of the same image. For each instance of the specific space filling curve, we compute the amplitude metric, d_a. Recalling that a small amplitude metric implies a good alignment of features, we choose the space filling curve that has the smallest amplitude metric.

Black areas in Figures 5(a-c) correspond to zero lightness or zeros of the function $l(s)$. In aligning $l_2(s)$ (simulation) to $l_1(s)$ (observation), the zero values can move large distances to align nonzero peaks in the functions. This movement is reflected in the deformed space filling curve shown in Figure 5(c). For this application, we are not interested in the movement of the zeros. Using the lightness channel of the 1D image as a weight, we create a weighted displacement field to represent the motion needed to align features in the 2D images. The displacement from simulation to observation is $\mathbf{x} \circ \gamma^{*-1} - \mathbf{x}$. The weighted displacement has the form $l_2(s)(\mathbf{x} \circ \gamma^{*-1} - \mathbf{x})/D$. The constant scale D is chosen to ensure that vector magnitudes are represented in the color space. For example, D can be the maximum magnitude of the vector field in the figure. Or, to keep the color consistent over several images, D could be the maximum possible vector length for all images (the image size). Figure 5(d) shows the weighted vector displacement, which is now localized to the crack. The displacements show a rotation with the upper

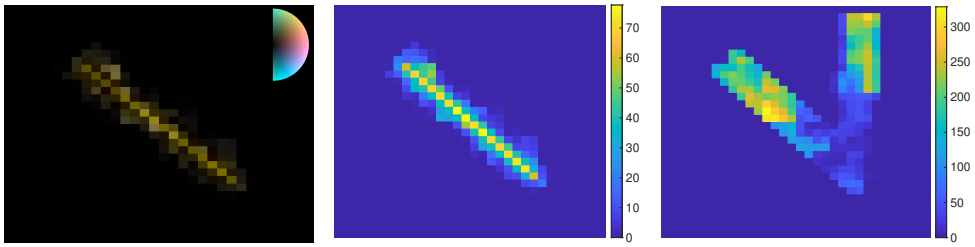

(a) Color Difference (b) ΔE (c) ΔP

Figure 6: Differences between Figure 5(a) and (c). The color difference in (a) uses crack orientations in $(-\pi/2, \pi/2]$ that are doubled to obtain the hue; (b) is the color difference metric; and (c) is a phase distance measure.

part of the simulation crack moving further than the lower part to align with the observation. Note, we can also align in the opposite direction, from observation to simulation, in which case the weighted displacement would be $l_1(s)(\mathbf{x} \circ \gamma^* - \mathbf{x})/D$.

3.5. Image Amplitude and Phase

It is of interest to develop metrics on images that mimic the one-dimensional phase and amplitude separation in Equation [7]. In this section, we work toward developing such metrics. A rigorous analysis of images requires restricting the set of images, $\mathcal{I}$, to those whose pixels can be put in one-to-one correspondence with the nodes of a SFC(n), for a given, fixed order n. The amplitude distance between images $I_1, I_2 \in \mathcal{I}$ should measure the difference in the images once I_2 is aligned with I_1. The data for such a metric would come from comparing Figure 5(c) to Figure 5(a) in this crack example. As previously noted, the L_2 distance between colors, Equation [2], has meaning in the L*Ch color space. Figure 6(a) shows the color difference between the observation, Figure 5(a), and the warped simulation, Figure 5(c). Since both cracks have constant magnitude and orientation, the yellow ($\pi/4$) orientation of the observation minus the pink zero orientation of the simulation, results in the yellow difference in Figure 6(a). In warping I_2 to I_1, each point of the observation image with coordinates $\mathbf{x}(s)$ has a color triplet associated with it, $(l_1(s), c_1(s), h_1(s))$, giving the lightness, chroma, and hue. The corresponding warped simulation image has a triplet $(l_2 \circ \gamma(s), c_2 \circ \gamma(s), h_2 \circ \gamma(s))$ at the same coordinate. These data are used to compute a color difference $\Delta E(s)$ at each point according to Equation [2], a contour plot of which is in

Figure 6(b). A corresponding amplitude metric, $D_{a,\gamma}$, for the entire image is obtained by integrating ΔE over the domain of the two image curves $I_1(s)$ and $I_2(\gamma(s))$. In the discrete setting, this reduces to a sum over the N nodes $s_1, s_2, \ldots, s_N$, defining the space filling curve

$$D_{a,\gamma}(I_1, I_2) = \sqrt{\frac{1}{N}\sum_{i=1}^{N} \Delta E^2(s_i)}, \text{ where } \gamma \text{ warps } I_2 \text{ to } I_1 \tag{8}$$

If I_1 is warped to I_2, the color comparison is between $(l_2(s), c_2(s), h_2(s))$ and $(l_1 \circ \gamma^{-1}(s), c_1 \circ \gamma^{-1}(s), h_1 \circ \gamma^{-1}(s))$. The substitution $s = \gamma(t)$ shows that $D_{a,\gamma}(I_1, I_2) = D_{a,\gamma^{-1}}(I_2, I_1)$. When $\gamma = \gamma_{id}$, where γ_{id} is the identity warping, $\gamma_{id}(s) = s$, $D_{a,\gamma_{id}}$ is the image amplitude metric for the original, unaligned images. Since ΔE is a metric on colors, it is straightforward to verify $D_{a,\gamma}$ is a metric on images.

A phase metric should measure the effort required to warp one image into the other. A candidate phase metric is a measure of the weighted displacement field, an example of which is in Figure 5(d). However, using the lightness as a weight would include amplitude information in the phase. Moreover, the weighted displacement from I_2 to I_1 would not be the same as from I_1 to I_2. An alternative is to weight the displacement by the Heaviside function, H, of the lightness, where $H(x) = \begin{cases} 1 & x > 0 \\ 0 & x = 0 \end{cases}$. Averaging the displacement from I_2 to I_1 and from I_1 to I_2 provides a symmetric measure

$$\Delta P(s) = \frac{1}{2}\left(H(l_1(s))\|\mathbf{x} \circ \gamma^*(s) - \mathbf{x}(s)\|^2 + H(l_2(s))\|\mathbf{x} \circ \gamma^{*-1}(s) - \mathbf{x}(s)\|^2\right) \tag{9}$$

Figure 6(c) shows a contour plot of ΔP for the crack example. This defintion of ΔP quantifies the size of the displacement needed to align the two images for the subset of pixels in the images with nonzero lightness. For this reason, we refer to ΔP as a phase distance measure.

A corresponding image phase distance measure is obtained by integrating over the domain

$$D_p(I_1, I_2) = \sqrt{\frac{1}{N}\sum_{i=1}^{N} \Delta P(s_i)}. \tag{10}$$

D_p is symmetric and non-negative. It is zero if and only if ΔP is zero, in which case γ^* is the identity and the two images have the same lightness but

the chroma and hue can differ. This defect could be corrected by considering the metric to be defined on the equivalence class of images with the same lightness. However D_p does not satisfy the triangle inequality, which is a harder defect to overcome, and thus is not a metric on the space of images. Further refinement is needed, but this measure has proven to be useful temporarily in developing the calibration framework illustrated in Sec. 3.6.

3.6. Parameterized Crack Example

This example is devised to illustrate how the image amplitude and phase metrics might be used to perform parameter calibration. Secondarily, this example shows that cracks can be aligned over a range of positions and orientations within an image. We create multiple images containing a single crack with fixed magnitude and length but the crack is rotated and shifted within the image domain. The rotation or the orientation of the crack is represented by the angle between the normal of the crack and the x-axis. The cracks are parameterized by two parameters, (a, b), where a is the distance shifted along the diagonal of the image, ranging from -0.25 to 0.25 in an image of size one, and b is the crack orientation varying from $-\pi/2$ to $\pi/2$. Each image contains a single crack as shown in Figure 7(a), where the thumbnail image is placed according to its parameter values (a, b). The horizontal axis corresponds to the parameter a and the vertical axis to b. Crack orientation changes going top to bottom, and crack position changes from left to right.

Instead of a uniform sampling of the parameter space we use a Latin Hypercube Sampling with 80 cases. This sampling provides parameter values that do not lie along rows and columns in parameter space, and helps to minimize sampling bias while exploring effectiveness of the metrics. We view these 80 crack cases in this parameter domain as simulation cases and we define the observation to be the case at $(0, \frac{\pi}{4})$ which is indicated by the red star in Figure 7. We want to see if the functional alignment through the space filling curves and the resulting metrics is meaningful.

Figure 7(b) plots the warped simulations for each parameter setting. The process and the metrics used across the parameter space have been highlighted for the specific case illustrated in Figure 5 and the associated measures in Figure 6. Over all parameters, we see the warped simulation cases look very similar to the observation in position and color lightness, but the hue varies. This result is expected since the warping is performed based only on the lightness, with chroma and hue brought along without change. In fact,

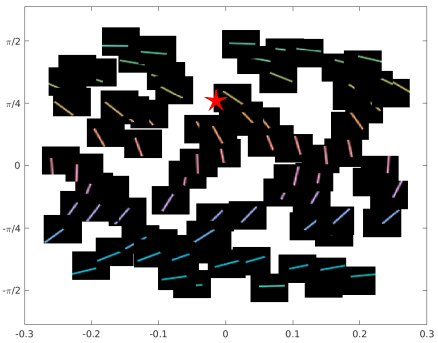

(a) Simulation

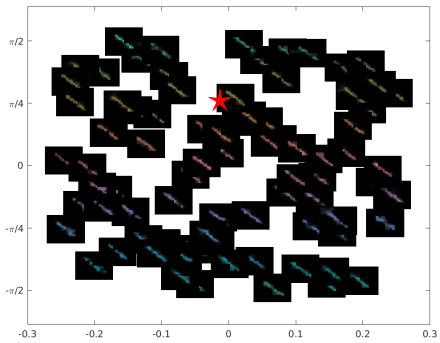

(b) Warped Simulation

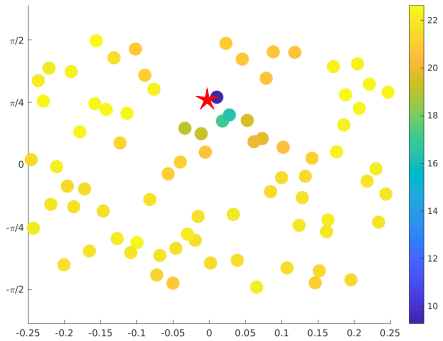

(c) $D_{a,\gamma_{id}}$

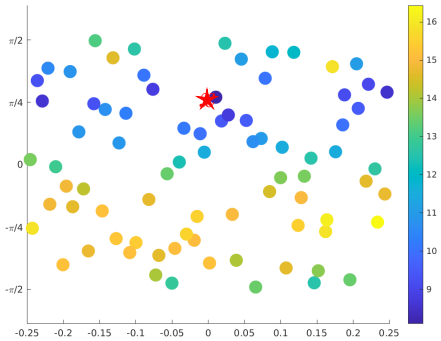

(d) D_{a,γ^*}

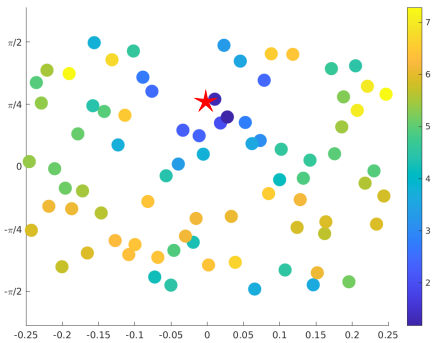

(e) D_p

Figure 7: Multi-crack analysis.

the hue in Figure 7(b) is roughly constant along rows since the vertical-axis parameter controls the crack orientation. Image alignment is good throughout the range of orientation and position parameters. To quantify the difference between the now aligned images we plot the unaligned image amplitude metric, $D_{a,\gamma_{id}}$, for all simulation cases in Figure 7(c) and the aligned image amplitude metric D_{a,γ^*} in Figure 7(d). As previously noted, comparing unwarped images, $D_{a,\gamma_{id}}$, gives no information; whereas the amplitude metric based on image warping, D_{a,γ^*}, is minimized around the correct parameter settings defining the observation, indicating little difference between the warped image and the observation image. The image amplitude metric is similar along rows in the parameter domain which reflects the observed differences in hue shown in Figure 7(b). The image phase, D_p, is shown in Figure 7(e) where larger values indicate larger warping needed for cases further from the observation and small values when little warping is needed to align the images. Note the colors are periodic in the vertical direction for Figures 7(b,d), because the orientation, and therefore hue, is periodic.

The fact that the image amplitude and phase measures are minimized near the observation shows that these measures hold promise as tools for parameter calibration. It should be noted that the calibration is performed on the metrics and not directly on the images themselves. Working with the metrics drastically reduces the problem size, and provides a highly efficient calibration framework.

4. Conclusions

The principal motivation for the CIEL*Ch color space is that it is designed so that equal L_2 distances between color codes results in equal perceived color differences. Thus renderings using this color map provide reliable visual cues for physically meaningful differences. Moreover, computations on the color codes reflect measures on the vectors themselves. More precisely, we have shown that the color map defines a non-Euclidean metric on two-dimensional vectors that combines information from three skill measures. Section 2.1 looks at visualization of a smooth vector field obtained from monthly-averaged, daily sea ice motion in the Arctic. The color is used to focus attention on two different flow patterns that tend to arise in the Arctic. Differences in these patterns are also highlighted using a difference color map associated with the vector metric introduced in this paper.

At a local scale, sea ice motion often results in fractures forming in the ice. Comparing simulation results using fracture models with observation is difficult because fractures are discrete localized features that are not likely to be coincident in both the observation and simulation. Image warping can be used to compare discrete, localized features. However, warping two-dimensional images is numerically tricky and analytically less convenient than the similar process of aligning functions. Section 3.2 introduces the idea of sampling a two-dimensional image using a space filling curve in order to transform two-dimensional image warping into the more reliable functional alignment problem. Results are presented using idealized fractures to show that image alignment is possible and accurate using space filling curves. Moreover, a new image-based amplitude metric and phase distance measure show promise as tools in parameter calibration. However, work remains. The proposed image phase measure needs to be modified to form a proper metric. Further, it is unclear if using the Heaviside function of the lightness to weight the displacement in the phase measure is appropriate in other applications. These issues remain subjects for future investigation.

Acknowledgments

This work was supported by the Laboratory Directed Research and Development program at Sandia National Laboratories, a multi-mission laboratory managed and operated by National Technology and Engineering Solutions of Sandia, LLC, a wholly owned subsidiary of Honeywell International, Inc., for the U.S. Department of Energy's National Nuclear Security Administration under contract DE-NA0003525.

This material is also based upon work supported by the U.S. Department of Energy, Office of Science, Office of Basic Energy Research under Award Number DE-SC0023366.

by the United States Government or any agency thereof. The views and opinions of authors expressed herein do not necessarily state or reflect those of the United States Government or any agency thereof.

The authors thank Oleksii Beznosov for pointing us to the use of space filling curves in image processing.

References

[1] A. H. Murphy, R. L. Winkler, A general framework for forecast verification, Monthly Weather Review 115 (1987) 1330–1338.

[2] D. Crosby, L. C. Breaker, W. H. Gemmel, A proposed definition of vector correlation in geophysics: Theory and application, Journal of Atmospheric and Oceanic Technology 10 (1993) 355–367.

[3] R. W. Grumbine, Long range sea ice drift model verification, NOAA/NWS/EMC/MMAB Contribution no. 135 (2012) 1–21.

[4] M. R. Luo, CIELAB, in: R. Luo (Ed.), Encyclopedia of Color Science and Technology, Springer, Berlin, Heidelberg, 2014, pp. 1–7. URL: https://doi.org/10.1007/978-3-642-27851-8_11-1.

[5] Y. Guan, C. Sampson, J. Tucker, W. Chang, A. Mondal, M. Haran, D. Sulsky, Computer model calibration based on image warping metrics: an application for sea ice deformation, Journal of Agricultural, Biological and Environmental Statistics 24 (2019) 444–463.

[6] D. H. Laidlaw, R. M. Kirby, C. D. Jackson, J. S. Davidson, T. S. Miller, M. Da Silva, W. H. Warren, M. J. Tarr, Comparing 2d vector field visualization methods: A user study, IEEE Transactions on Visualization and Computer Graphics 11 (2005) 59–70.

[7] T. Munzner, Visualization Analysis & Design, CRC Press, Florida, 2015.

[8] K. Thyng, C. Greene, R. Hetland, H. Zimmerle, S. DiMarco, True colors of oceanography: Guidelines for effective and accurate colormap selection, Oceanography 29 (2016) 9–13. doi:dx.doi.org/10.5670/oceanog.2016.66.

[9] A. W. Kruse, A. S. Alenin, J. S. Tyo, Review of visualization methods for passive polarization imaging, Opt. Eng. 58 (2019) 082414–1–17. doi:10.1117/1.OE.58.8.082414.

[10] M. Tschudi, W. N. Meier, J. S. Stewart, C. Fowler, J. Maslanik, Polar Pathfinder Daily 25 km EASE-Grid Sea Ice Motion Vectors, Version 4., Technical Report, Boulder, Colorado USA. NASA National Snow and Ice Data Center Distributed Active Archive Center, 2019.

[11] Y. Zhao, A. K. Liu, Arctic Sea-Ice Motion and Its Relation to Pressure Field, Journal of Oceanography 63 (2007) 505–515.

[12] T. Urness, V. Interrante, E. Longmire, I. Marusic, S. O'Neill, T. W. Jones, Strategies for the visualization of multiple 2d vector fields, IEEE Computer Graphics and Applications 26 (2006) 74–82. doi:10.1109/MCG.2006.88.

[13] A. A. Goshtasby, Image Registration: Principles, Tools, and Methods, Springer-Verlag London, 2012.

[14] M. Beg, M. Miller, A. Trouve, L. Younes, Computing large deformation metric mappings via geodesic flows of diffeomorphisms, International Journal of Computer Vision 61 (2005) 139–157.

[15] H. Tagare, D. Groisser, O. Skrinjar, Symmetric non-rigid registration: A geometric theory and some numerical techniques, Journal of Mathematical Imaging and Vision 34 (2009) 61–88.

[16] T. Vercauteren, X. Pennec, A. Perchant, N. Ayache, Diffeomorphic deomons: Efficient non-parametric image registration, NeuroImage 45 (2009) S61–S72.

[17] Q. Xie, A. Srivastava, Image registration using phase-amplitude separation, Variational Methods (2016) 83–106.

[18] A. Srivastava, E. Klassen, S. Joshi, I. Jermyn, Shape analysis of elastic curves in Euclidean spaces, IEEE Transactions on Pattern Analysis and Machine Intelligence 33 (2011) 1415–1428.

[19] M. F. Mokbel and W. G. Aref, Irregularity in multi-dimensional space-filling curves with applications in multimedia databases, in: Proceedings

of the Tenth International Conference on Information and Knowledge Management, CIKM '01, Association for Computing Machinery, New York, NY, USA, 2001, pp. 512–519.

[20] R. Dafner, D. Cohen-Or, Y. Matias, Context-based space filling curves, in: Computer Graphics Forum, volume 19, Wiley Online Library, 2000, pp. 209–218.

[21] M. F. Mokbel, W. G. Aref, I. Kamel, Analysis of multi-dimensional space-filling curves, GeoInformatica 7 (2003) 179–209.

[22] A. Srivastava, E. P. Klassen, Functional and shape data analysis, Springer, 2016.

[23] A. Srivastava, W. Wu, S. Kurtek, E. Klassen, J. S. Marron, Registration of functional data using Fisher-Rao metric, arXiv (2011) 1103.3817.

[24] J.D. Tucker and W. Wu and A. Srivastava, Generative models for functional data using phase and amplitude separation, Computational Statistics & Data Analysis 61 (2013) 50–66.